

Using geomagnetic birefringence to locate sources of  
impulsive, terrestrial VHF signals  
detected by satellites on orbit

Abram R. Jacobson (corresponding author)  
&  
Xuan-Min Shao

Space and Atmospheric Sciences Group  
Mail Stop D466  
Los Alamos National Laboratory  
Los Alamos, New Mexico 87545 USA  
ajacobson@lanl.gov

to be submitted to: Radio Science

Los Alamos National Laboratory report LA-UR-00-3991

## Abstract

The Earth's ionosphere is magnetized by the geomagnetic field and imposes birefringent modulation on VHF radio signals propagating through the ionosphere. Satellites viewing VHF emissions from terrestrial sources receive ordinary and extraordinary modes successively from each broadband pulse emitted by the source. The birefringent inter-mode frequency separation can be used to determine the value of  $f_{ce} \cos \theta$ , where  $f_{ce}$  is the electron gyrofrequency and  $\theta$  is the angle between the wavevector  $\mathbf{k}$  and the geomagnetic field  $\mathbf{B}$  at the point where the VHF raypath intersects the ionosphere. Successive receptions of multiple signals (from the same source) cause variation in  $f_{ce} \cos \theta$ , and from the resulting variation in the signal inter-mode frequency separation the source location on Earth can be inferred. We test the method with signals emitted by the Los Alamos Portable Pulser and received by the FORTE satellite.

## Introduction

This article proposes a new method for determining the location on Earth of impulsive radio emissions, by exploiting the characteristics of signals acquired by radio receivers aboard Earth-orbiting satellites. The new method is not related either to interferometric direction-finding or to time-of-arrival (TOA) methods. Instead, the new method takes advantage of the signal modulation imposed by the radio-frequency birefringence of the Earth's ionosphere.

Satellites are the only platform for global collection of Very-High-Frequency (VHF; 30 – 300 MHz) radiation, which is not ducted over the horizon by the ionosphere. VHF emanations from sources beyond the horizon cannot be monitored by ground-based sensors. A single satellite fares poorly at determining the latitude and longitude (geolocation) of a source in the low VHF. The satellite antenna lobe angular width is  $\sim \lambda/D$  (radians), where  $\lambda$  is the radio wavelength and  $D$  is the antenna aperture. At 30 MHz ( $\lambda = 10\text{m}$ ), even a deployed 10-m antenna would have a beam of  $\sim 1$  radian width, which is quite poor for geolocation. For a low-Earth-orbit (LEO) satellite to achieve even crude 100-km resolution at nadir from 1000-km altitude, an extremely expensive 100-m deployed antenna would be required. The alternative is to fly a satellite constellation, with at least three satellites required to geolocate the source by TOA techniques. In either case, geolocation resolution drives the mission cost to escalate nonlinearly.

Many radio-frequency signals, such as those emanating from lightning storms, occur repetitively during the passage of a LEO satellite within view of the source or source

cluster. During such a series of signal repetitions from the same location, the LEO satellite ( $\sim 100$ -minute orbital period) moves relative to the source. The rf line-of-sight at each instant in the orbit passes from the source, through the Earth's ionosphere, to the satellite. The rf signal is dispersed in the ionospheric plasma, and the dispersed signal is further separated into “magneto-ionic” modes [Budden, 1988] of radio propagation due to the plasma's birefringence. To first approximation, the instantaneous frequency separation of the two modes (at any given time in the received waveform) is  $2f_{ce} \cos \theta$ , where  $f_{ce}$  is the electron-cyclotron frequency, proportional to magnetic field (2.80 MHz per gauss), and  $\theta$  is the angle between the field  $\mathbf{B}$  and the rf wavevector  $\mathbf{k}$ . This forms the basis for cumulative inference of the source location: As the satellite receives subsequent repetitions of signal from the same source but with the receiver at different orbital positions, the observable inter-mode frequency separation  $2f_{ce} \cos \theta$  changes in a predictable way that depends on source and satellite locations. The latter is known, and the former can be uniquely retrieved.

### **The concept**

The ionospheric plasma disperses a radio pulse as it propagates from the ground to a satellite. Consider an impulsive, broadband radio emission from a location on the surface, or near the surface of, the Earth. The pulse essentially fills the frequency bandwidth of the radio receiver. In the absence of geomagnetic birefringence, the index of refraction would be approximately [Budden, 1988] given by

$$\mu = 1 - \frac{1}{2} \frac{f_p^2}{f^2} \quad (1)$$

where  $f_p$  is the plasma frequency and  $f$  is the radio frequency. Here we have assumed that  $f_p^2 \ll f^2$ , as is readily the case in this work, where the effective passband employed by the FORTE receivers is  $f=26$  to 48 MHz, while typically the plasma frequency is in the range 3 to 8 MHz. The group delay for propagation is

$$\tau = \frac{1}{2\pi} \frac{dk}{df} ds \quad (2)$$

where  $k$  is the wavenumber and  $ds$  is the path element along the propagation path. From Eqs. (1) and (2) we obtain

$$\tau = \frac{R}{c} + \frac{1}{2c} \frac{f_p^2}{f^2} ds = \frac{R}{c} + \frac{\alpha N}{f^2} \quad (3)$$

Here,  $R$  is the straight-path distance from the source to the satellite,  $c$  is the speed of light in vacuum,  $N$  (in  $\text{m}^{-2}$ ) is the slant total electron content along the straight path,  $\alpha$  is  $1.34 \times 10^{-7}$ , and  $f$  is the frequency (in Hz). We may invert Eq. (3) to express the frequency as a function of time during the dispersed "chirp" received at the satellite:

$$f = \sqrt{\frac{\alpha N}{t - t_0}} \quad (4)$$

where  $t_0$  is the time of arrival in lieu of ionospheric dispersion. Eq. (4) shows the increasingly delayed arrival time of as the frequency is reduced. Put another way, the higher frequencies in the passband arrive earlier, and the lower frequencies arrive later.

This analysis can be extended to include the effect of the Earth's dipole magnetic field. This field varies (in magnitude and direction) gradually versus position, on a spatial scale comparable to the Earth's radius, while the ionospheric F-layer (where most ionospheric density resides) is only ~100 to 200 km thick, or a few percent of the Earth's radius. The birefringence is generated only where there is significant plasma density, that is, within the relatively thin shell (on the scale of the magnetic field variations) represented by the F-layer. That is why we are justified in treating the birefringence as if the ionosphere were a thin layer, of path-integrated density  $N$ , located at the altitude of the F-layer, and as if the birefringence occurred for the value of the vector magnetic field where the radio propagation path (line-of-sight) pierces that layer. Performing this analysis [Massey *et al.*, 1998], we find that the dispersive arrival of frequencies is described by

$$f = \sqrt{\frac{\alpha N}{t - t_0}} \pm f_{ce} \cos \beta \quad (5)$$

$f_{ce}$  is the electron gyrofrequency (in Hz), and  $\beta$  is the angle between the wavevector  $\mathbf{k}$  and the geomagnetic field  $\mathbf{B}$ , at the point where the line-of-sight pierces the F-layer. The "-" sign is for the ordinary mode, while the "+" sign is for the extraordinary mode [Budden,

1988]. In practice, the ionospheric F-layer dominates the accumulated refractivity, so the appropriate value of  $f_{ce} \cos \theta$  in Eq. (5) is that near the peak of the F-layer.

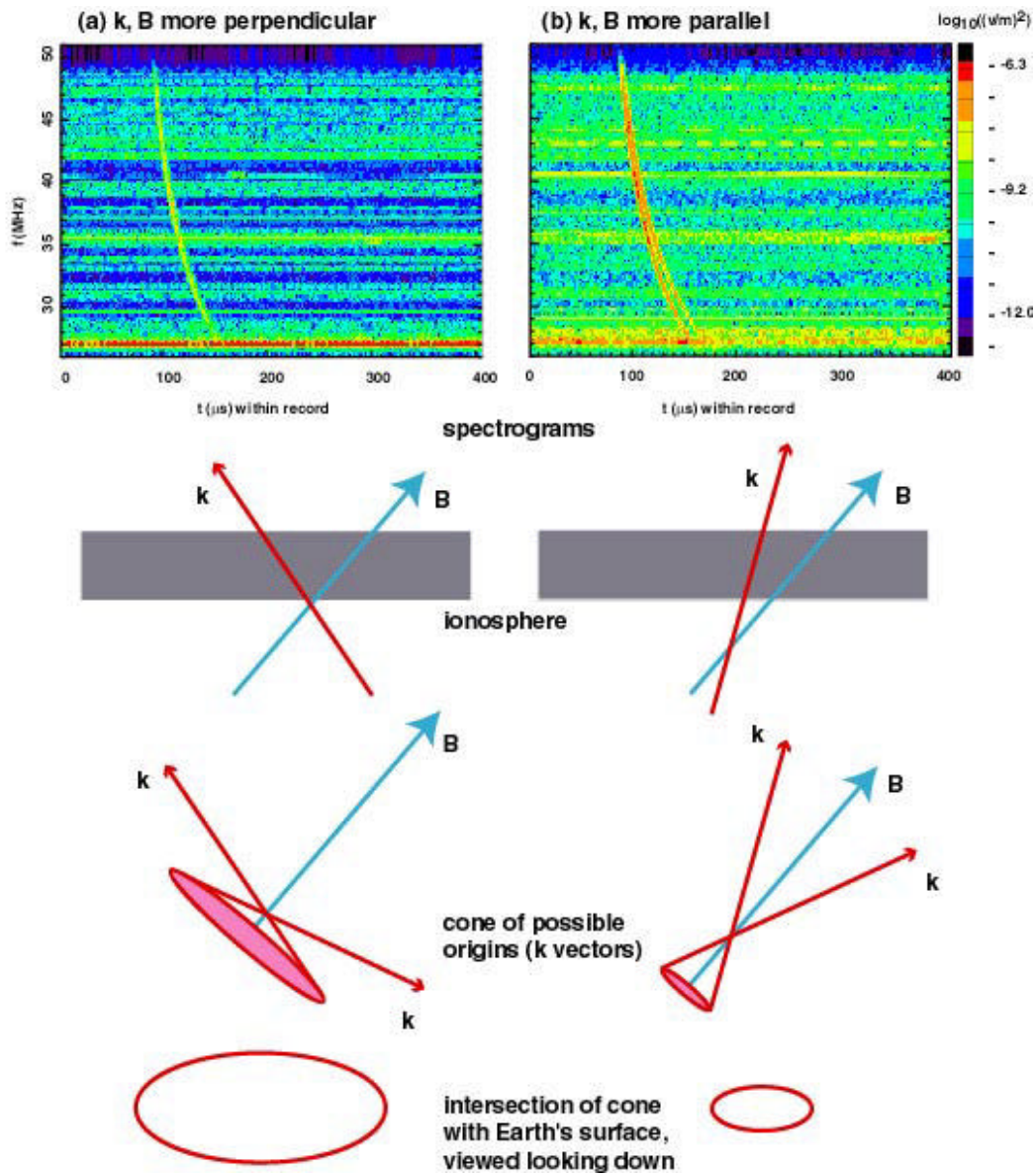
Eq. (5) is derived under the "quasilongitudinal approximation", which is valid only where  $|\cos \theta / \sin^2 \theta| \gg f_{ce}/(2f)$  [Budden, 1988]. If we take  $f_{ce}=0.3$  MHz and  $f=30$  MHz, then we require  $|\cos \theta / \sin^2 \theta| \gg 0.3$  degrees. That is, the approximation breaks down only within a degree of  $\mathbf{k}$  and  $\mathbf{B}$  being exactly orthogonal. Thus the quasilongitudinal approximation is robustly satisfied for essentially all of our data.

The effect of birefringence can be described as the simultaneous arrival of energy at frequencies  $f \pm f_{ce} \cos \theta$ . At any given time, energy at the frequency  $f + f_{ce} \cos \theta$  is from the extraordinary mode, while energy at the frequency  $f - f_{ce} \cos \theta$  is from the ordinary mode. (*In the absence of the geomagnetic field*, the energy that would be arriving at this time would have the *single* frequency  $f$ .) Provided the source is linearly polarized, a particularly efficient way of extracting  $f_{ce} \cos \theta$  is to measure the beat frequency between the extraordinary and ordinary modes. For unpolarized sources, the methods of extracting  $f_{ce} \cos \theta$  are slightly more cumbersome but are nonetheless straightforward.

The key concept in this proposal is that measurement from one satellite location of  $f = 2f_{ce} \cos \theta$  constrains the possible locations of the source on Earth. Figure 1 shows the situation for two possible orientations of the  $\mathbf{k}$  vector with respect to the same  $\mathbf{B}$  vector: (a) In the left column,  $\mathbf{k}$  is less parallel to  $\mathbf{B}$ , i.e. the angle  $\theta$  is closer to  $90^\circ$ . (b) In the right column,  $\mathbf{k}$  is more parallel to  $\mathbf{B}$ , i.e. the angle  $\theta$  is closer to  $0^\circ$ . The spectrograms in

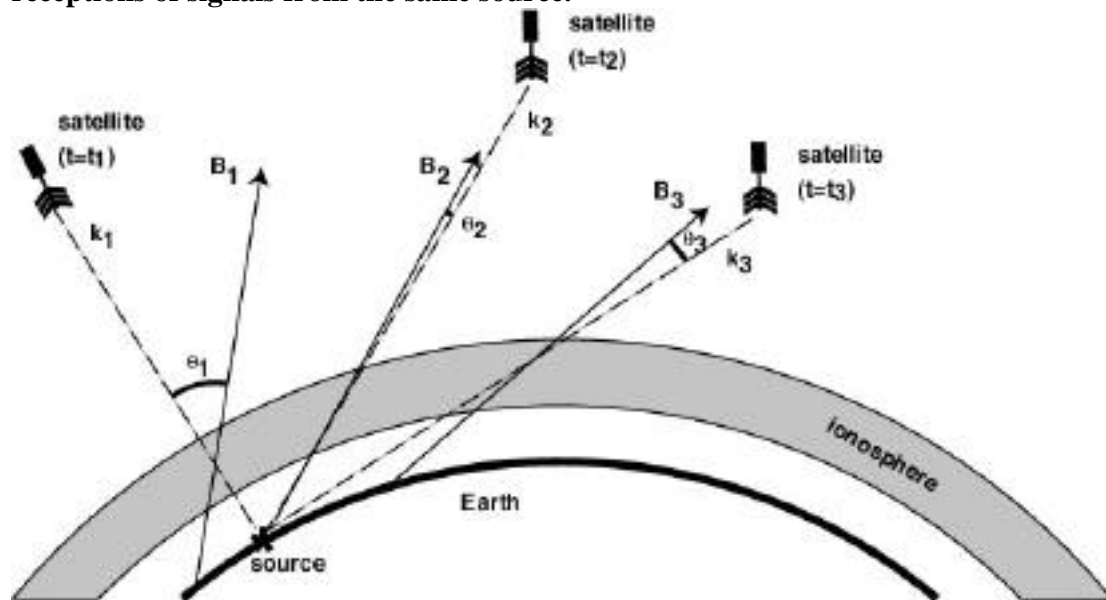
the top row are real data from the FORTE satellite [*Jacobson et al.*, 1999] illuminated by the Los Alamos Portable Pulser, a broadband, high-power VHF impulsive source [*Massey et al.*, 1998]. In each case, as in all data to be used in this study, the passband is effectively 22 to 48 MHz (although the full Nyquist passband extends to 53 MHz.) The spectrogram in (a) shows less mode separation. The spectrogram in (b) shows more mode separation. The second row (both a and b) shows a cartoon of the ionospheric interaction region, where the inter-mode frequency separation occurs. The third row (both a and b) shows a cartoon of the cones of possible  $\mathbf{k}$  vectors consistent with the measured values of  $f = 2f_{ce} \cos \theta$ . The bottom row (both a and b) shows a cartoon of those cones' intersections with the Earth's surface. The source is inferred to lie on such a curve of intersection.

Figure 1: Comparison of birefringence-based location constraints for (a)  $k$ ,  $B$  more perpendicular, and (b)  $k$ ,  $B$  more parallel. Top row: Spectrograms of LAPP impulses received by FORTE. The overall  $f^2$  dispersion is due to ionospheric plasma. The inter-mode frequency separation (see right column) is due to geomagnetic birefringence. Second row: Angular relation of  $k$ ,  $B$  within ionosphere. Third row: Cones of possible arrival directions based on geomagnetic constraint. Bottom row: Intersection of those cones with the Earth's surface.



Next, how can these constraints be combined to yield a point geolocation? This is done by combining data from at least three repeated emissions, from separated satellite positions. Figure 2 is a cartoon of the collection of three separate VHF signals from the same source on Earth. Each signal propagates through the ionosphere's principal layer, where it makes an angle with the geomagnetic field  $B$ .

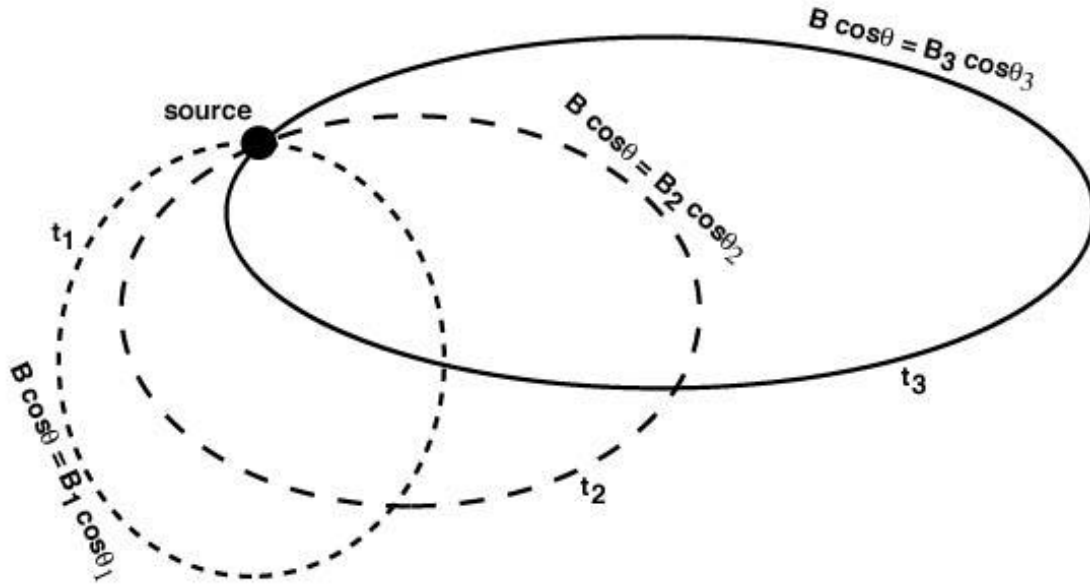
**Figure 2: Relationship of  $k$ ,  $B$  within ionosphere for three successive satellite receptions of signals from the same source.**



For each position of the satellite, the received signal's inter-mode frequency separation tags the pertinent value of  $f_{ce} \cos \theta$ , indicating a cone on which the source must lie. Each cone's intersection with the Earth's surface is a closed curve and is shown in cartoon form in Figure 3. The source location is inferred to be at the intersection of the three closed curves. (In this respect the present geomagnetic approach to inferring location gives a graphical endproduct that is analogous to the isochrones of TOA.) The only

possibility of two-fold ambiguity would occur if the satellite orbital plane coincided with a magnetic meridian plane; however such a case would be rare.

**Figure 3: Closed curves of source location constraints (on surface of the Earth) for the three lines-of-sight shown in Figure 2. Note the unique intersection corresponding to the source location.**



A remarkable feature of the present approach to geolocation is that the cone-intersection curves can be amassed cumulatively over time, each curve being stored in an archive which would be periodically opened and searched for common intersections. The detailed waveforms don't have to be the same between repeated receptions; they just have to possess enough bandwidth to enable retrieval of  $f = 2f_{ce} \cos \theta$ . This is a fundamental advantage over TOA, allowing attribution to be inferred *a posteriori* from a cumulative archive of closed curves on a map of the Earth's surface.

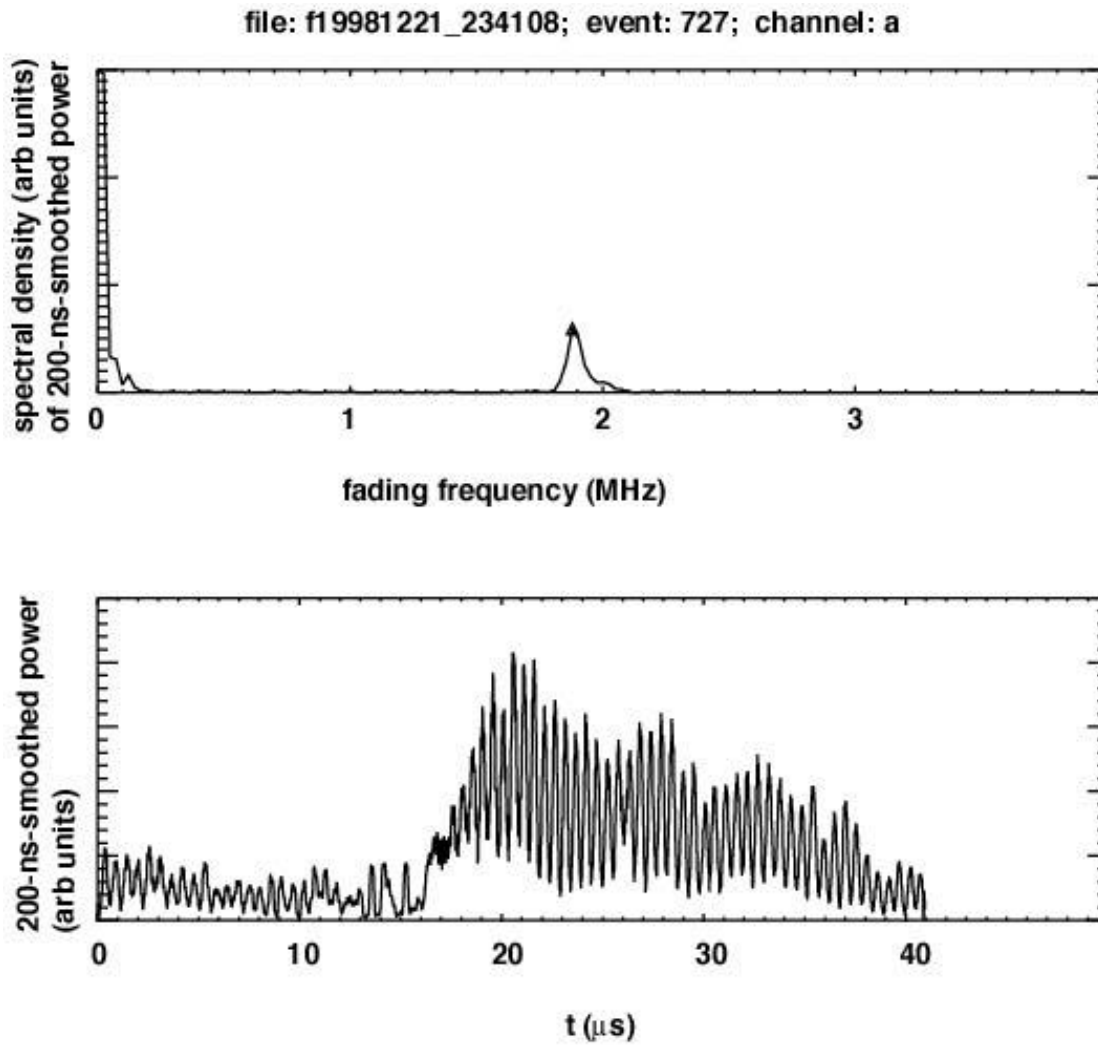
### Test of the geolocation concept

The FORTE satellite has collected impulsive signal waveforms from the LAPP on more than one-thousand occasions [Jacobson *et al.*, 1999]. The data used here will be those FORTE signals from LAPP illuminations in which the data were acquired by the 50-Megasample-per-second receiver set to cover the range 26-51 MHz, i.e. the FORTE "low band" [Jacobson *et al.*, 1999].

For each LAPP signal in this low band, we analyze 40  $\mu$ s of data centered on the arrival time of the pulse. Eq (5) shows that if we square the signal, the *square* will manifest an amplitude modulation at beat frequency  $f = 2f_{ce} \cos \theta$ , due to the interference between the extraordinary and ordinary modes. To exploit the beating for retrieval of  $f_{ce} \cos \theta$ , after squaring the signal we smooth the squared signal by averaging within a sliding 0.2- $\mu$ s window, then take the power spectrum of the smoothed squared signal. The peak in the power spectrum, provided there is a significant peak, will reveal the parameter  $f = 2f_{ce} \cos \theta$ .

Figure 4 shows this for one event. The lower panel shows the smoothed square of the signal, while the upper panel shows the power spectrum of the smoothed square of the signal. The smoothed square of the signal is modulated, almost fully, at a frequency of about 1.9 MHz. The peak at 0 MHz in the power spectrum is related to the overall offset and can be ignored; the modulation causes the second peak at 1.9 MHz. Evidently then the parameter  $f_{ce} \cos \theta$  is approximately 0.95 MHz.

**Figure 4: Amplitude-modulated power data from a single LAPP impulse received by FORTE's 26-51 MHz passband receiver. Lower panel: Power averaged in sliding, 200-nanosec window. Upper panel: Power spectrum of 200-nanosecond-averaged power.**



The quality of the fading spectral peak (see top panel of Figure 4) varies somewhat amongst the FORTE recordings of LAPP signals. We have chosen simply to select the peak of the spectrum as the indicator of  $2f_{ce} \cos \theta$ , but we do not mean to imply that this choice is necessarily better than using a power-weighted determination of the spectral

peak. The fact that the peak has some measurable width is not predicted by the simplified arguments leading to Eq. (5) and must indicate some inaccuracies in our approximate model. In general, our experience with LAPP signals recorded by FORTE indicates that the intrinsic uncertainty in the measurement of  $2f_{ce} \cos \theta$ , as indicated by the spectral width of the fading peak, is at least 0.03 MHz (best case) and frequently deteriorates to 0.15 MHz. We surmise that the failure of the peak to be a perfectly narrow spike (on the frequency axis) as would be suggested by our simplified model is due to (a) finite signal-to-noise ratio, (b) imprecision of the thin-shell ionosphere model, (c) imprecision of the quasilongitudinal approximation, and (d) higher-order (i.e., quartic) effects in the basic ionospheric dispersion as a function of  $1/f$ .

To analyze the entire set of FORTE low-band LAPP signal collections, we impose a signal-to-noise requirement on the power spectrum (see upper panel in Figure 4): We require that the secondary peak in the frequency range 0.3 to 3.0 MHz exceed the median level in that frequency range by a factor of at least 20. This results in a set of only 628 acceptable low-band LAPP signals contributing to what follows. (The rest of the LAPP signals did not achieve this signal-to-noise-ratio in their amplitude modulation.)

These 628 LAPP signals were intermittently gathered by FORTE over a campaign covering more than a year. Most of the collections were during daylight, but the season, solar activity, and geomagnetic-storm conditions varied widely. Therefore we do not expect the ionospheric effective altitude to have been perfectly constant during the collection of all our data; it may have varied over the range 250 to 500 km during this

campaign. Nonetheless, this variability in expected effective altitude remains small compared to the spatial scale (the Earth's radius) over which  $\mathbf{B}$  varies, so we are somewhat justified in comparing our data to a standard-altitude ionosphere model. However, we must bear in mind that this model is only approximate, as is, for that matter, the assumption that we may treat the ionosphere as a thin shell.

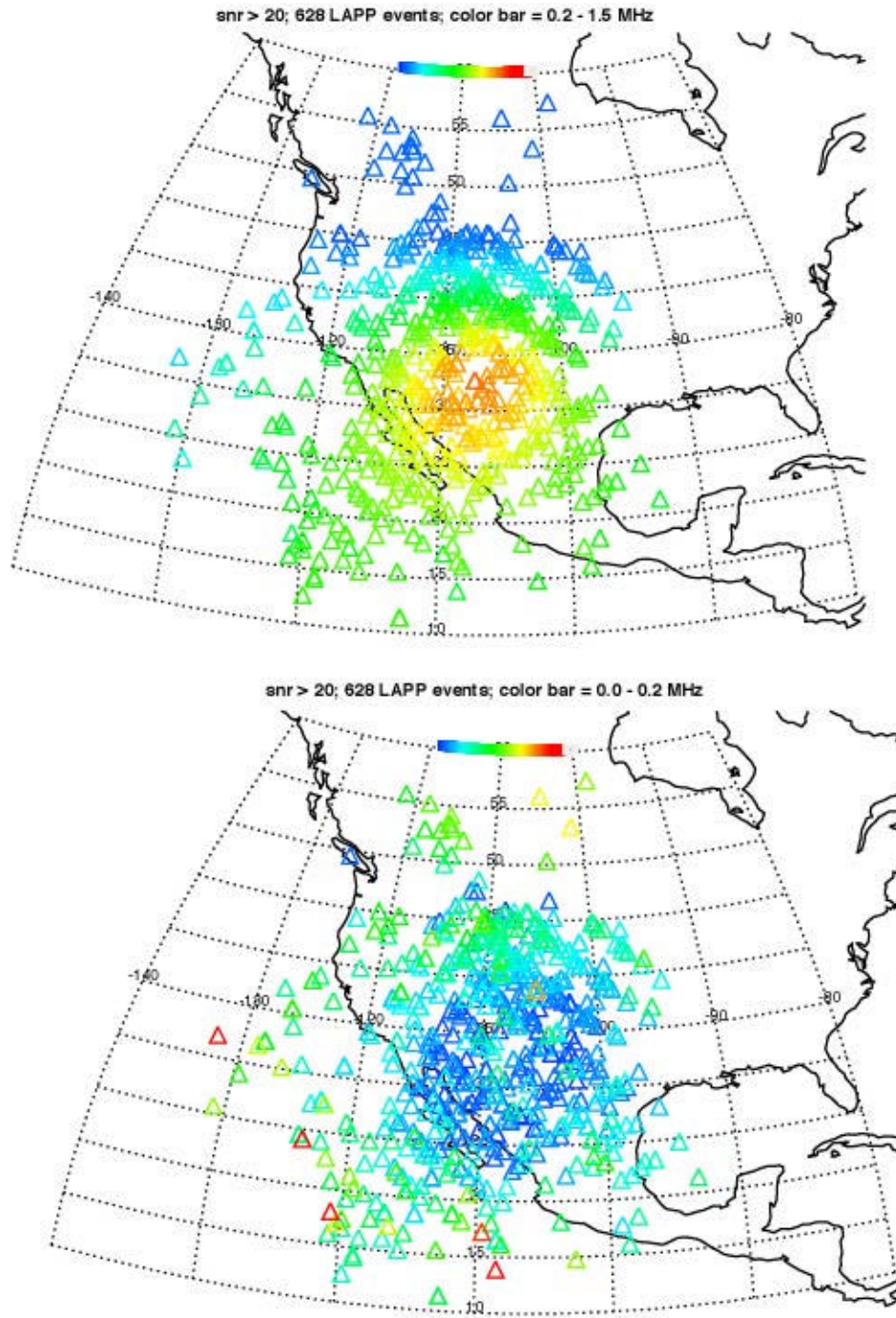
Figure 5 shows a map of the subsatellite location (longitude, latitude) for these 628 acceptable signal recordings of LAPP impulses. The top panel encodes the retrieved value of  $f_{ce} \cos \theta$  as the color of the data point, ranging from 0.2 to 1.5 MHz (see upper color bar). The warmer (yellow, amber)-colored data points have lines of sight to the LAPP (which is at 35.87 deg N, -106.33 deg E) that are optimally aligned with  $\mathbf{B}$  in the ionospheric F-layer, resulting in the highest values of  $f_{ce} \cos \theta$  for this data set. The coldest (blue)-color data points are for lines of sight to the LAPP that are closer to being normal to  $\mathbf{B}$  within the ionospheric F-layer. It is this position-dependent heterogeneity of retrieved values of  $f_{ce} \cos \theta$  that allows an inference of the source location.

The lower panel of Figure 5 encodes the absolute value of the difference between measured (see upper panel) and modeled  $f_{ce} \cos \theta$  for this data set. The model is the International Geomagnetic Reference Field [Barton, 1997] updated to 1995. This model is appropriate below the magnetosphere. In our use of the IGRF, we choose 400 km above the Earth as the effective height at which to evaluate  $f_{ce} \cos \theta$ . This is an approximation of the entire ionospheric propagation as being equivalent to a penetration of one effective annular layer at 400 km. We have also varied the assumed height and

found the results to be only weakly affected for the height within a range 250-500 km. A more precise approach would be to evaluate an integral of the refraction over a range of ionospheric heights. However, it will turn out (see below) that our errors are dominated not by the thin-ionosphere assumption but rather by ray-bending.

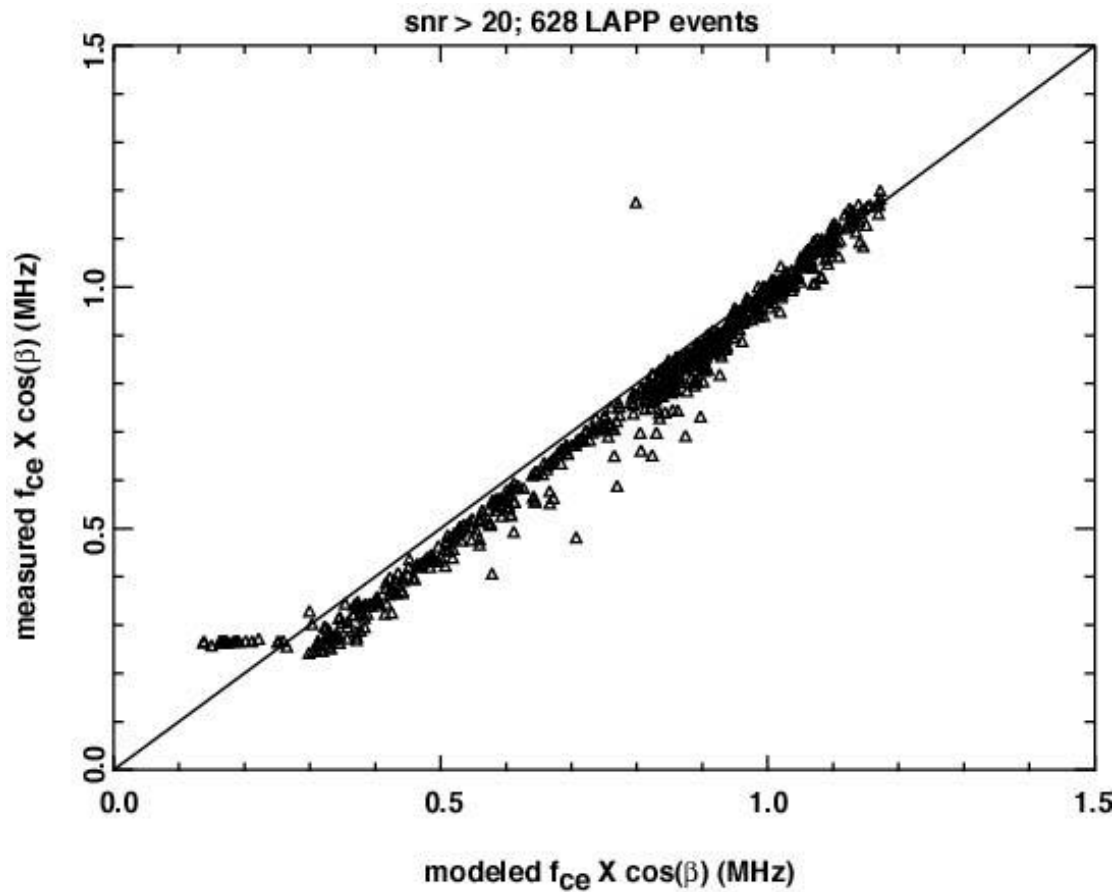
The lower panel of Figure 5 shows that the discrepancies between the measurements and the model of  $f_{ce} \cos \theta$  tend to be small in magnitude ( $<0.05$  MHz) for high-elevation-angle lines of sight and/or for  $\cos \theta$  near unity, and tend to be larger in magnitude (up to or occasionally exceeding 0.1 MHz) for low-elevation-angle lines of sight and/or low values of  $\cos \theta$ . This basic feature does not change if we vary the assumed ionospheric altitude (for evaluation of  $f_{ce} \cos \theta$  in the model) within a reasonable range (250-500 km).

**Figure 5: Map of subsatellite points during 628 accepted LAPP-impulse receptions. Top panel: Color coding of inferred  $f_{ce} \cos\beta$  from the pulse birefringence. Bottom panel: Magnitude of measured  $f_{ce} \cos\beta$  minus modeled  $f_{ce} \cos\beta$ , assuming a 400-km effective ionospheric layer height.**



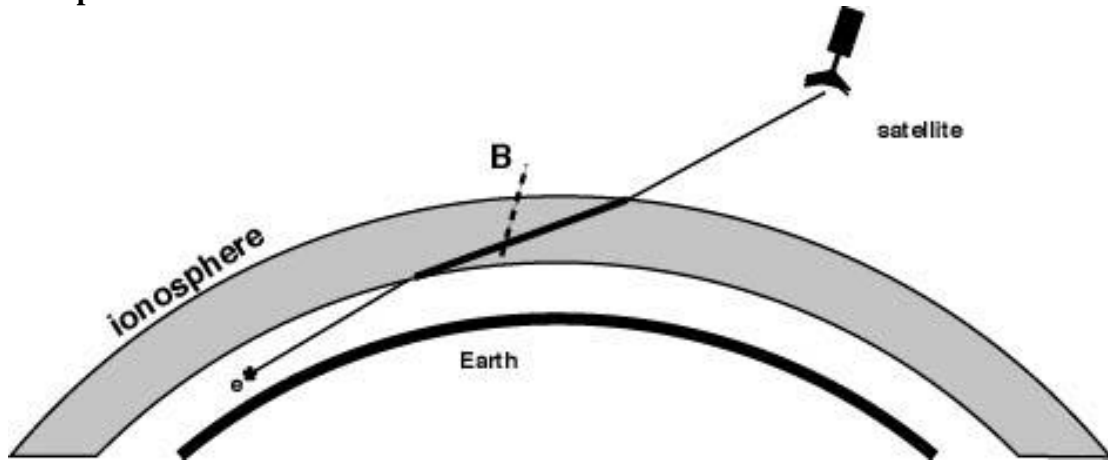
A way to gain better insight into the data/model discrepancies is to graph the measured versus the model results, as is done in Figure 6. The solid line indicates equality. Evidently the discrepancies are least for large values of  $f_{ce} \cos \beta$ , i.e. for close alignment of  $\mathbf{k}$  and  $\mathbf{B}$ . Similarly, the errors are larger for smaller values of  $f_{ce} \cos \beta$ , i.e. for near-orthogonality of  $\mathbf{k}$  and  $\mathbf{B}$ . Note also that the errors tend to be of one sign: The measured  $f_{ce} \cos \beta$  tends to be smaller than the modeled  $f_{ce} \cos \beta$ , with the exceptions of one outlier and several points at the lowermost values of modeled  $f_{ce} \cos \beta$ .

**Figure 6: Measured  $f_{ce} \cos \beta$  (vertical axis) versus modeled  $f_{ce} \cos \beta$  (horizontal axis), assuming a 400-km effective ionospheric layer height.**



What distinguishes the majority of the data (for which the measured  $f_{ce} \cos \beta$  is below the model values) from the several points at the far left (for which the measured  $f_{ce} \cos \beta$  is *above* the model values)? It turns out that there is a simple discriminant, tending to implicate raybending as the dominant source of these measurements/model discrepancies. Figure 7 shows a cartoon of raybending. Since the radio-frequency phase index of refraction is less than unity, a ray incident from the emitter ("e") tends by Snell's Law to be bent into a more grazing angle (heavy segment of raypath) through the ionosphere. Also shown in Figure 7 is the geomagnetic field direction (dashed line) evaluated at the ionospheric ray transit. Evidently the effect of raybending in the case shown here will be to increase the angle between  $\mathbf{k}$  and  $\mathbf{B}$ , i.e. to reduce the measured  $f_{ce} \cos \beta$  below the model value calculated as if raybending did not occur. *Moreover, the sensitivity of measured  $f_{ce} \cos \beta$  to raybending maximizes for  $\beta$  close to 90 deg.*

**Figure 7: Cartoon of ionospheric raybending, for the majority case in which the effect of raybending is to widen the angular separation between  $\mathbf{k}$ ,  $\mathbf{B}$  within ionosphere.**



It so happens that each of the data points in Figure 6 (see above) for which the measured  $f_{ce} \cos \theta$  is below the model value also has a nominal raypath lower in elevation angle than  $B$ , as shown in Figure 7. Thus, for those majority events, the increasing discrepancy between measured and modeled  $f_{ce} \cos \theta$  (as  $\cos \theta$  is reduced) is precisely what we would expect based on the effect of raybending. Moreover, the several points on the far left of Figure 6, for which the measured  $f_{ce} \cos \theta$  is *above* the model value, all turn out to have the opposite arrangement of  $B$  and  $k$ ; that is, the effect of raybending is to increase  $f_{ce} \cos \theta$  *above* the model value. The clear implication is that ionospheric raybending might be producing the dominant error in the retrievals of  $f_{ce} \cos \theta$ . (We cannot explain the single outlier point by this argument.)

The argument so far has shown that raybending is consistent with the trends in Figure 6. In order to make credible the role of raybending in producing the actual residuals shown by Figure 6, we need also to show that the expected raybending order-of-magnitude at least suffices to generate the order-of-magnitude residuals effects we see. What matters is the deviation of the raypath from the nominal line-of-sight direction, within the F-layer. Snell's Law provides that

$$u \sin \theta_{ext} = \sin \theta_{int} \quad (6)$$

is the relation of the incidence angle (off of normal) both external and internal to the ionosphere. Hence the raybending internal to the ionosphere, relative to the nominal line-of-sight, is given by

$$\delta\theta = (\mu - 1)\tan\theta_1 \quad (7)$$

With reference to the situation in Figure 7, let us suppose that the plasma frequency in the ionosphere is  $f_p = 5$  MHz. Then the index of refraction in the plasma (see Eq. 1) for a radio frequency of 30 MHz will be  $\mu = 1 - 0.014 = 0.986$ . Thus in this example the refractive angular deviation (in radians) in the ionosphere will be  $\delta\theta = 0.014 \times \tan\theta_1$ .

On the other hand, the residual in  $f_{ce} \cos\beta$  due to raybending through an angle  $\delta\theta$  will be

$$\delta(f_{ce} \cos\beta) = -f_{ce} \delta\beta \sin\beta \quad (8)$$

Thus the *fractional* variation in  $f_{ce} \cos\beta$  due to raybending through an angle  $\delta\theta$  will be

$$\frac{\delta(f_{ce} \cos\beta)}{(f_{ce} \cos\beta)} = -\delta\beta \tan\beta \quad (9)$$

Noting that the largest value of  $\delta\theta$  will be  $\theta_1$ , we can substitute Eq. (7) into Eq. (9) to get

$$\frac{\delta(f_{ce} \cos\beta)}{(f_{ce} \cos\beta)} = (1 - \mu)\tan\beta \tan\theta_1 \quad (10)$$

in terms of magnitudes.

Inspecting Figure 6, we see that the *fractional* residual at in the lower quarter of the plot is in the range 0.1 to 0.2. Noting that  $1-\mu=0.014$ , we see that Eq. (10) requires that  $\tan \theta \tan \theta_1$  be on the order of 10 for this to be satisfied. This is very easy to do with reasonable parameters, for example if both  $\theta$  and  $\theta_1$  were 72 degrees. Thus we conclude that refractive raybending is not only implicated by the trend in the systematic residuals of Figure 6, but also is easily capable of generating the required magnitudes of angular deviation.

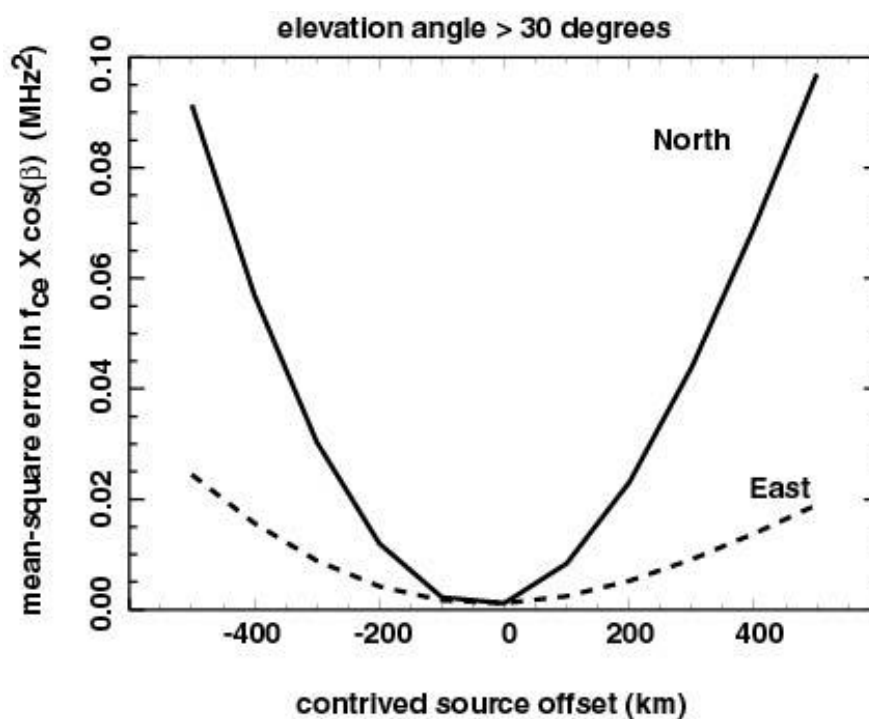
### **Test for accuracy of geolocation**

The data from these 628 events can be used to examine the possible accuracy of source geolocation through this novel geomagnetic method. To do this, we limit our attention to those lines-of-sight higher than 30 deg in elevation (seen from the source), so that we somewhat reduce the effects of raybending. This still, it turns out, provides enough data "leverage" to allow successful, and rather accurate, geolocation, albeit still affected by ray-bending.

To test the geolocation, we introduce an array of contrived source-position errors, first a set of north-south errors, and then a set of east-west errors, in 100-km steps out to  $\pm 500$  km in both cases. Figure 8 shows the mean-square residuals for each such scan. The measurements of  $f_{ce} \cos \theta$  do not change, but the model results of  $f_{ce} \cos \theta$  do change, as a result of our inserting the contrived source-location errors. The curves of square residuals

clearly minimize within a few tens of km of the true source position, and the curvature of the square residuals about their minima indicate that the positional resolution is less than 50 km north south, and perhaps 100 km east-west. Moreover, the north-south square residuals are minimized by placement of the source 30-40 km *north* of the true source location. This can be shown to be a systematic effect of raybending, especially of the lines-of-sight to the north of the LAPP but within the 30-degree elevation-angle acceptance cone.

**Figure 8: Response of mean-square residuals (in  $f_{ce} \cos\beta$ ) for north/south (solid curve) and east/west (dashed curve) contrived errors in source location.**



## Conclusions

The new method of geolocation presented here is based on measurement of  $f_{ce} \cos \beta$  via the complex signal modulation imposed on broadband VHF signals as they transit the

ionosphere. The method is limited to signals in the low VHF, because the birefringent inter-mode frequency separation varies as  $f^3$ , and higher frequencies would lack sufficient sensitivity. Moreover, the method is limited to repetitive signals which can be viewed by a satellite at several positions in the satellite orbit. One example of broadband signals which can be viewed repetitively by a satellite at several orbital positions is the VHF signatures of lightning. There may be anthropogenic radio emitters locatable in this manner as well.

We have tested the method using a dataset based on anthropogenic broadband radio emissions from the Los Alamos Portable Pulser at 35.87 deg N, -106.33 deg E. Analysis of the dataset indicates that the primary source of error in this method of geolocation is likely to be ionospheric raybending. Analysis also indicates that positional accuracies of tens of km (on the Earth's surface) may be expected for reasonably high-quality data. This is adequate, for example, to allow association of VHF lightning signatures with specific storm-system features in geostationary-satellite visible and infrared imagery.

## **Acknowledgements**

The work described here was performed under the auspices of the United States Department of Energy. We are indebted to the FORTE operations team, led by Phil Klingner and Diane Roussel-Dupré, for constant support in acquiring and working with FORTE data. We are also indebted to David Smith and Daniel Holden for operation of the LAPP facility.

## References

Barton, C.E., International Reference Geomagnetic Field: the seventh generation, *J. Geomag. Geoelectr.*, 49, 121-146, 1997.

Budden, K.G., *The Propagation of Radio Waves*, 667 pp., Cambridge University Press, Cambridge, 1988.

Jacobson, A.R., S.O. Knox, R. Franz, and D.C. Enemark, FORTE observations of lightning radio-frequency signatures: Capabilities and basic results, *Radio Sci.*, 34 (2), 337-354, 1999.

Massey, R.S., S.O. Knox, R.C. Franz, D.N. Holden, and C.T. Rhodes, Measurements of transionospheric radio propagation parameters using the FORTE satellite, *Radio Sci.*, 33 (6), 1739-1753, 1998.